Physics of Plasmas

RESEARCH ARTICLE | NOVEMBER 03 2022

# Dephasing and phase-locking: Dual role of radial electric field in edge MHD dynamics of toroidally confined plasmas

Y. Zhang ; Z. B. Guo ; P. H. Diamond ; X. Q. Xu ; Z. Y. Li ; M. Xu



*Physics of Plasmas* 29, 112101 (2022)
https://doi.org/10.1063/5.0105360

Physics of Plasmas ARTICLE scitation.org/journal/php

# Dephasing and phase-locking: Dual role of radial electric field in edge MHD dynamics of toroidally confined plasmas

Cite as: Phys. Plasmas **29**, 112101 (2022); doi: 10.1063/5.0105360
Submitted: 23 June 2022 · Accepted: 23 September 2022 ·
Published Online: 3 November 2022



Y. Zhang,[1,2] Z. B. Guo,[2,a)] P. H. Diamond,[3] X. Q. Xu,[4] Z. Y. Li,[5] and M. Xu[1]

## AFFILIATIONS

[1]Southwestern Institute of Physics, PO Box 432, Chengdu 610041, China
[2]State Key Laboratory of Nuclear Physics and Technology, Fusion Simulation Center, School of Physics, Peking University, Beijing 100871, China
[3]University of California San Diego, La Jolla, California 92093, USA
[4]Lawrence Livermore National Laboratory, Livermore, California 94551, USA
[5]Oak Ridge Associated University, Oak Ridge, Tennessee 37831, USA

[a)]Author to whom correspondence should be addressed: zbguo@pku.edu.cn

## ABSTRACT

We carry out several numerical simulations to illustrate how the radial electric field ($E_r$) impacts the edge magnetohydrodynamic (MHD) instabilities. The analyses reveal that $E_r$-shear ($E_r'$, here the prime denotes the derivative with respect to the radial direction) tends to stabilize the kink/Peeling–Ballooning modes by dephasing the perturbed radial velocity ($\tilde{v}_r$) and displacement ($\tilde{\xi}_r$). However, $E_r$-curvature ($E_r''$) tends to destabilize the kink/peeling modes by inducing a phase lock between $\tilde{v}_r$ and $\tilde{\xi}_r$. More specifically, the ratio between them could be measured to quantify their relative competition strength. Consequently, the shape of $E_r$ is crucial to the shape of linear growth rate spectrum $\gamma(n)$ (here $n$ is the toroidal mode number), which further determines the nonlinear dynamics. On the one hand, relatively larger $E_r$-curvature causes narrower $\gamma(n)$, leading to larger nonlinear energy loss fraction. On the other hand, relatively larger $E_r$-shear has the opposite effect.



## I. INTRODUCTION

In nature, waves exist widely, such as gravity waves in the ocean,[1] Rossby waves in the atmosphere,[2] Alfvén waves in the solar wind,[3] drift waves in the tokamaks,[4] etc. These waves arise from the fact that there are gradients in the background profiles, and they will propagate due to vorticity anomalies across the interface. Thus, they all can be called vorticity waves and may interact, leading to instabilities.[5] In fluid systems, shear flow instability can be interpreted as the interaction of two (or more) vorticity waves, which are driven by vorticity gradients. The fundamental mechanism is that the vorticity waves can achieve phase locking and mutual amplification.[6] This novel interpretation goes beyond the classical eigenvalue method, since it can only assess the basic state to be stable or unstable. Intuitively, in magnetohydrodynamic (MHD) systems, there are many other different free energy sources: current gradient, pressure gradient, and so forth. All of them can produce local vorticity waves and they will interact with each other. An interesting problem immediately arises: how these vorticity waves couple and form a joint mode? Therefore, it is significant to extend this "new" concept to provide a physically based understanding of the nonintuitive MHD instabilities.

In toroidally confined tokamak experiments, the radial electric field ($E_r$) is a key element for transition from low confinement mode (L-mode) to high confinement mode (H-mode), which is a reference scenario for ITER operation.[7,8] Once we achieve H-mode, if the gradient of equilibrium pressure or current is too large, some MHD instabilities such as kink/peeling and ballooning instability may break out.[9] One typical "explosive" instability is the edge localized mode (ELM), and it is bad for confinement.[10] Generally speaking, MHD instabilities in tokamaks may lead to complete plasma collapse if it is treated carelessly. Hence, one is more interested in searching for stable equilibria or methods that can suppress or mitigate these instabilities. By using neutral beam injection or other strategies,[11,12] we could modify the $E_r$ profile to relax transport in a continuously quasisteady process rather than an intermittent violent one, which is important for determining

access to different ELM-free states (QH mode,[13] EDA-H mode,[14] I-mode,[15] etc).[16] The main two components to form a "U" shape $E_r$ profile are $E_r$-shear ($E_r'$) and $E_r$-curvature ($E_r''$). In the low density QH mode regime, it is often accompanied by coherent edge harmonic oscillation (EHO). In high density EDA-H mode regime, there often appears quasi-coherent modes. These (quasi-)coherent modes usually localized in the steep edge gradient region,[17–19] where the $E_r$-shear is small but the $E_r$-curvature is large. Remarkably, the $E_r$-shear usually mitigates the ballooning modes[20] or turbulence transport,[21–23] while the $E_r$-curvature (which is related to vorticity gradient) may drive shear flow instability from fluid dynamics point of view.[6] We speculate that the $E_r$-curvature may be possibly associated with these (quasi-)coherent modes, which stimulated our interest to address their underlying relationships and physics. The joint mode instability in the edge tokamak has been reviewed in Ref. 24, and this paper presents more details and extensions.

The rest of this paper is organized as follows: in Sec. II, we introduce our basic model of reduced MHD equations. In Sec. III, we present typical numerical simulations to describe vortex-kink mode in the MHD framework. The further linear and nonlinear simulations in Sec. IV are mainly about the impact of $E_r$-shear and $E_r$-curvature on Peeling–Ballooning instability. Finally, brief conclusions and discussions are given in Sec. V.

## II. BASIC MODEL

In this work, we use the three-field nonlinear two-fluid reduced MHD equations under the BOUT++ framework to construct simulations,[25,26] which could include the hyper-resistivity,[26] K–H term,[27] ion diamagnetic drift, and gyroviscosity.[28] This model describes the evolutions of perturbed vorticity $\tilde{\omega}$, pressure $P$, and parallel vector potential $A_{||}$ within flute reduction $k_{||}/k_\perp \ll 1$

$$\frac{d\tilde{\omega}}{dt} = -\boldsymbol{v_1}\cdot\nabla\bar{\omega}_0 + B_0\nabla_{||}J_{||} + 2\boldsymbol{b_0}\times\kappa_0\cdot\nabla P, \tag{1}$$

$$\frac{dP}{dt} + \boldsymbol{v_1}\cdot\nabla P_0 = 0, \tag{2}$$

$$\frac{\partial A_{||}}{\partial t} = -\partial_{||}\Phi + \frac{\eta}{\mu_0}\nabla_\perp^2 A_{||} - \frac{\eta_H}{\mu_0}\nabla_\perp^4 A_{||}, \tag{3}$$

$$\tilde{\omega} = \frac{\rho_0}{B_0}\left(\nabla_\perp^2\tilde{\phi} + \frac{\nabla_\perp^2 P_i}{n_0 Z_i e}\right), \quad \bar{\omega}_0 = \frac{\rho_0}{B_0}\nabla_\perp^2\Phi_{V0}, \tag{4}$$

$$J_{||} = J_{||0} - \frac{1}{\mu_0}\nabla_\perp^2 A_{||}, \tag{5}$$

$$\Phi = \Phi_0 + \tilde{\phi} = \Phi_{dia0} + \Phi_{V0} + \tilde{\phi}, \tag{6}$$

where $d/dt = \partial/\partial t + \boldsymbol{V_{E\times B}}\cdot\nabla, \nabla_{||}F = B\partial_{||}(F/B), \partial_{||} = \boldsymbol{b}_0\cdot\nabla + \tilde{\boldsymbol{b}}\cdot\nabla, \tilde{\boldsymbol{b}} = \nabla A_{||}\times\boldsymbol{b}_0/B$, and $\kappa_0 = \boldsymbol{b}_0\cdot\nabla\boldsymbol{b}_0$. The $\boldsymbol{E}\times\boldsymbol{B}$ convection flow consists of three parts $\boldsymbol{V}_{E\times B} = \boldsymbol{V}_{E,dia0} + \boldsymbol{V}_{E,V0} + \boldsymbol{V}_1$, where $\boldsymbol{V}_{E,dia0} = \boldsymbol{b}_0\times\nabla\Phi_{dia0}/B$ balances the ion diamagnetic flow $\boldsymbol{b}_0\times\nabla P_{i0}/B$, $\boldsymbol{V}_{E,V0} = \boldsymbol{b}_0\times\nabla\Phi_{V0}/B$ corresponds to the net equilibrium flow, and $\boldsymbol{V}_1 = \boldsymbol{b}_0\times\nabla\tilde{\phi}/B$ is the perturbed flow with $\tilde{\phi}$ being the perturbed electrostatic potential. The net equilibrium flow is imposed by a hyperbolic tangent function[27]

$$V_{E,V0} = -\frac{E_{r,net}}{B} = R\frac{B_p}{B}\frac{d\Phi_{V0}(\psi)}{d\psi} = R\frac{B_p}{B}\left\{D_0\left[1-\tanh(D_s(\psi_{nor}-\psi_0))\right] + C\right\}, \tag{7}$$

where $\psi_{nor} = (\psi-\psi_{axis})/(\psi_{sep}-\psi_{axis})$ is the normalized radial coordinate, and $\psi_{axis}$ and $\psi_{sep}$ are magnetic fluxes at the magnetic axis and separatrix, respectively. $D_0$ controls flow amplitude, $D_s$ controls the flow shear, $\psi_0$ controls the flow location, and $C$ is a constant. The sign of $V_{E,V0}$ controls the flow direction. The three-field model is normalized through the plasma major radius at the magnetic axis $\bar{R}$, Alfvén time $\tau_A$, magnetic field intensity at the magnetic axis $\bar{B}$, and reference ion number density $n_0$, where $\tau_A = \bar{R}/V_A$, $V_A = \bar{B}/\sqrt{\mu_0 n_0 m_i}$ is the Alfvén velocity, $\mu_0$ is the permittivity in vacuum, and $m_i$ is the ion mass, respectively. Consequently, the time dependent variables are normalized as $\hat{P} = 2\mu_0 P/\bar{B}^2, \hat{\psi} = \psi/\bar{R}, \hat{\omega} = \tau_A\omega/(n_0 m_i), \hat{J}_{||} = -\mu_0\bar{R}J_{||}/\bar{B}, \hat{\phi} = \phi/(V_A\bar{R}\bar{B}), \hat{V} = V/V_A$. The grid numbers in the radial and poloidal direction are $n_x\times n_y = 516\times 64$ and in the toroidal direction is $n_z = 16$ for linear simulations and $n_z = 64$ for nonlinear simulations. To save simulation time and increase the efficiency, when performing nonlinear simulations with multi-mode initial perturbations,[29,30] only half torus is simulated and 16 harmonics are retained, which implies that the toroidal modes included are $n = 2i$ for $i = 0, 1, \ldots, 16$. In addition, the $n = 0$ net flow and $n = 0$ magnetic field generation are not included (i.e., set to zero) in the nonlinear simulations.

It should be noted that our system contains three drivers and two suppressors: the current gradient drives kink/peeling instability, the pressure gradient drives ballooning instability, and the vorticity gradient drives Kelvin–Helmholtz (KH) instability. The $E_r$-shear and magnetic shear usually suppress these instabilities. Generally, they are coupled and interact with each other to govern the edge dynamics. Due to the large bootstrap current in the steep pressure gradient region, where the $E_r$-shear and global magnetic shear is relatively weak,[27,31] some low-n instabilities may be destabilized by equilibrium vorticity or current gradient there. From the vorticity wave interaction's perspective, these drivers and suppressors would affect the global perturbed radial velocity and displacement, and then, the practical stability will change accordingly.

## III. VORTEX-KINK MODE

### A. Uniform mean profiles

Basically, the linear growth rate of instability can be expressed as

$$\gamma = \Re\left(\frac{\partial_t\tilde{\xi}_r}{\tilde{\xi}_r}\right) = \Re\left(\frac{\tilde{v}_r}{\tilde{\xi}_r}\right) = \frac{|\tilde{v}_r|}{|\tilde{\xi}_r|}\cos\left(\vartheta_{\tilde{v}_r} - \vartheta_{\tilde{\xi}_r}\right), \tag{8}$$

where $\tilde{v}_r = |\tilde{v}_r(\psi,t)|e^{i\vartheta_{\tilde{v}_r}(\psi,t)}e^{im\vartheta-in\zeta}$ and $\tilde{\xi}_r = |\tilde{\xi}_r(\psi,t)|e^{i\vartheta_{\tilde{\xi}_r}(\psi,t)}\times e^{im\vartheta-in\zeta}$ are the perturbed radial velocity and displacement, and $m$ and $n$ are poloidal and toroidal mode number, respectively. The key physics in Eq. (1) is that displacing the mean profiles results in interacting vorticity waves, which impact the perturbed velocity field and displacement.[24] The phase difference between $\tilde{v}_r$ and $\tilde{\xi}_r$ is crucial to the stability because it determines the system to be stable $[\cos(\vartheta_{\tilde{v}_r} - \vartheta_{\tilde{\xi}_r}) \le 0]$ or unstable $[\cos(\vartheta_{\tilde{v}_r} - \vartheta_{\tilde{\xi}_r}) > 0]$. Here, we construct several simulations with self-consistent simplified circular geometry equilibria to develop further understanding of the key physics. One is the mean flow destabilizes stable kink modes, and the other one is the mean flow stabilizes unstable kink modes. For the sake of simplicity, we did not include the evolution of the pressure perturbation [Eq. (2)], the curvature term [the third term on the right-hand-side (RHS) of Eq. (1)], and non-ideal effects (i.e., ion diamagnetic drift,

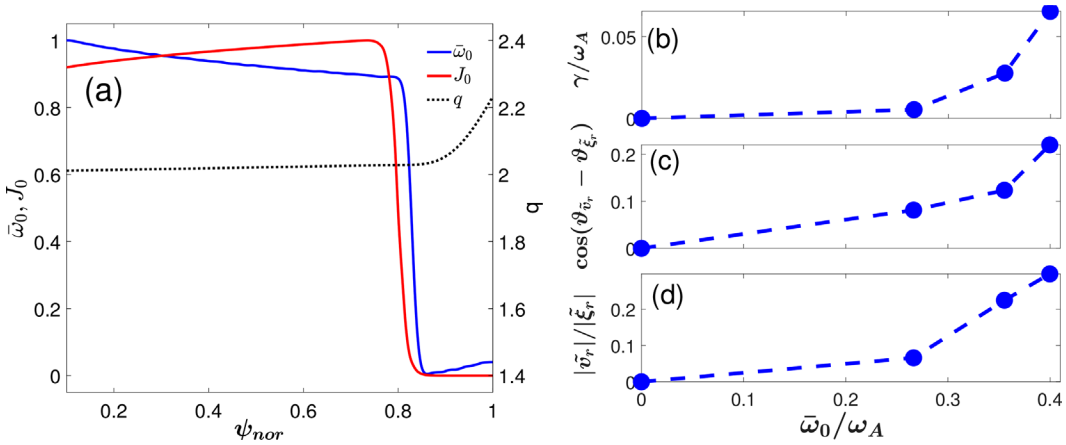


**FIG. 1.** Mean flow destabilizes stable kink modes: (a) the mean current, mean vorticity (which has been normalized to their maximum value) and safety factor $q$ profile, (b) the growth rate, (c) the corresponding spatially averaged cosine of cross phase $\vartheta_{\tilde{v}_r} - \vartheta_{\tilde{\xi}_r}$, where $\vartheta_{\tilde{v}_r}$ and $\vartheta_{\tilde{\xi}_r}$ are the phase of perturbed radial velocity and displacement, respectively, and (d) the corresponding spatially averaged amplitude ratio of $|\tilde{v}_r|$ to $|\tilde{\xi}_r|$. Here the toroidal mode number is $n = 1$.

gyroviscosity, resistivity, and hyper-resistivity). So, the ballooning drive is excluded in this section. In addition, we assumed a constant density as $n_0 = 5 \times 10^{19}\,\mathrm{m}^{-3}$ in this section. The normalized alfvén time is $\tau_A = 9.17 \times 10^{-7}$ s with the reference length $\bar{R} = 3.14$ m and magnetic field strength $\bar{B} = 1.57$ T, respectively. For the first case, Fig. 1 shows that the mean flow can destabilize the stable kink modes. Both the mean current and vorticity nearly have steep jumps, and the constant $q$ value is close to an integer 2 (so that the pure kink mode is stable for step like current profile[32]). The quantitative analyses show that the larger mean vorticity, the larger growth rate. Furthermore, we can see that the cosine of cross phase $\vartheta_{\tilde{v}_r} - \vartheta_{\tilde{\xi}_r}$ has a similar trend to the growth rate, meaning that increasing mean vorticity results in stronger phase-locking [i.e., larger $\cos(\vartheta_{\tilde{v}_r} - \vartheta_{\tilde{\xi}_r})$]. In the second case, Fig. 2 shows that the mean flow can stabilize the unstable kink modes, in which the constant $q$ value is far away from the integer 2 (so that the pure kink mode is unstable for step like current profile[32]). The results show that the larger mean vorticity, the smaller growth rate. In particular, only the cosine of cross phase $\vartheta_{\tilde{v}_r} - \vartheta_{\tilde{\xi}_r}$ has a similar trend to the growth rate, while the amplitude ratio $|\tilde{v}_r|/|\tilde{\xi}_r|$ indicates the opposite tendency. This phenomenon reveals that increasing mean vorticity results in stronger dephasing [i.e., smaller $\cos(\vartheta_{\tilde{v}_r} - \vartheta_{\tilde{\xi}_r})$], thus leading to smaller growth rate (i.e., stabilizing effect).

The main physics here is that the vorticity (flow shear) dephases the perturbed radial velocity and displacement while the vorticity gradient tends to align them.[24] For the step like drop of vorticity profiles, they contain vorticity and vorticity gradient, both of which will affect the stability behavior. The actual stability depends on their relative competition. In Fig. 1, the vorticity gradient dominates, so it destabilizes the stable kink mode. In Fig. 2, the vorticity dominates, leading to a stabilizing effect on the unstable kink mode. If we consider a constant vorticity profile, which means the effect of vorticity gradient is excluded, then we found that the results are similar to Fig. 2, i.e., the

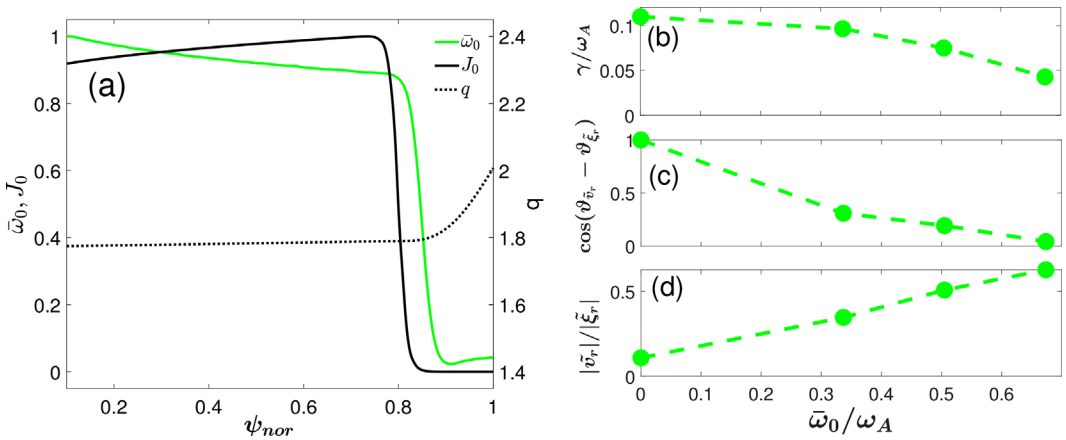


**FIG. 2.** Mean flow stabilizes unstable kink modes: (a) the mean current, mean vorticity (which has been normalized to their maximum value) and safety factor $q$ profile, (b) the growth rate, (c) the corresponding spatially averaged cosine of cross phase $\vartheta_{\tilde{v}_r} - \vartheta_{\tilde{\xi}_r}$, and (d) the corresponding spatially averaged amplitude ratio of $|\tilde{v}_r|$ to $|\tilde{\xi}_r|$. Here the toroidal mode number is $n = 1$.

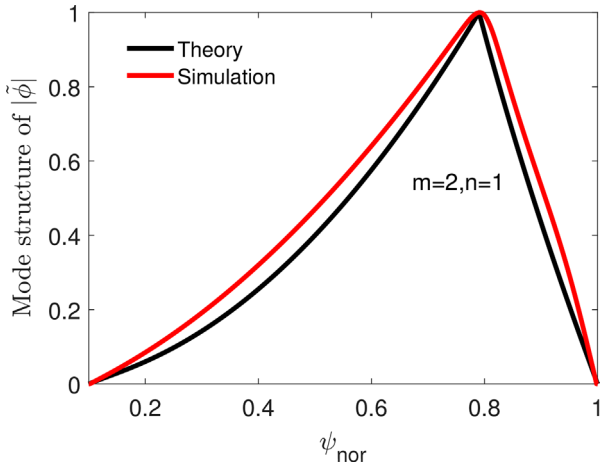


**FIG. 3.** Mode structure of the perturbed electrostatic potential for the $m = 2, n = 1$ kink mode. The red curve denotes the simulation results from BOUT++. The black curve denotes the theoretical mode structure based on Ref. 32 (pp. 65–70).

unstable kink mode will be stabilized. Furthermore, if the mean vorticity is increased to a larger value, e.g., $\bar{\omega}_0/\omega_A = 1.02$, there would not be an eigenmode anymore, and the (cosine of the) cross phase between perturbed radial velocity and displacement will become nonuniform and vary with space and time.[33]

It is worth mentioning that for step like current profiles, its linear stability of the driven kink modes is theoretically discussed through the reduced MHD equations.[32] For the case of Fig. 2, the poloidal mode structure of the pure unstable $m/n = 2/1$ kink mode ($\bar{\omega}_0/\omega_A = 0$ case) is shown in Fig. 3. As we can see, there is not too much difference between the theory and the simulation, and the discrepancy may be resulted from the fact that the current profile is not a completely step profile, the geometry is different and so forth. In addition, the flute reduction assumption by neglecting derivatives along the magnetic field line in the simulation model may have limitations in accurately calculating the n = 1 kink mode,[34] which indicates that the full-MHD model may be required for a further investigation.[35]

### B. Nonuniform mean profiles

Next, we construct linear simulations with nonuniform mean current and vorticity profiles, which will bring in magnetic shear. Figure 4 shows the mean parallel current profile and two different mean vorticity profiles. We know that different $E \times B$ mean flow corresponds to different $E_r$ profiles, the contained $E_r$-shear is related to the vorticity and the $E_r$-curvature is related to the mean vorticity gradient. To quantify the relative competition between the $E_r$-curvature and $E_r$-shear, we define a parameter $\mathcal{R}_{E_r}$

$$\mathcal{R}_{E_r} = \frac{\int_{\psi_{in}}^{1} |E_r''| d\psi}{\int_{\psi_{in}}^{1} |E_r'| d\psi} \Delta_w \approx \frac{\int_{\psi_{in}}^{1} |\bar{\omega}_0'| d\psi}{\int_{\psi_{in}}^{1} |\bar{\omega}_0| d\psi} \Delta_w, \tag{9}$$

where $\psi_{nor} = \psi_{in}$ and $\psi_{nor} = 1$ denote the position of inner radial boundary and separatrix, respectively. $\Delta_w = 1 - \psi_{in}$ is the width of integral length. For the two vorticity profiles in Fig. 4(b), we found that $\mathcal{R}_{E_r,flow1} > \mathcal{R}_{E_r,flow2}$, which means that the red curve (marked as "flow1") is $E_r$-curvature dominant, or in other words, the blue curve (marked as "flow2") is $E_r$-shear dominant. Figure 5 shows the Root-Mean-Square (RMS) of the perturbed electrostatic potential. It clearly reveals that the linear growth rate ($\gamma$) of $E_r$-curvature ($E_r$-shear) dominant case is larger (smaller) than that of the pure kink mode, i.e., $\gamma_{w/flow1} > \gamma_{w/o\,flow} > \gamma_{w/flow2}$. As a consequence, we can draw the conclusion that the $E_r$-curvature tends to destabilize while $E_r$-shear tends to stabilize the kink mode, leading to a joint "vortex-kink" mode.

## IV. IMPACT OF $E_r$-SHEAR AND $E_r$-CURVATURE

To go further and to be more general, we include the effect of equilibrium pressure gradient (i.e., ballooning effect), the pressure perturbation evolution and non-ideal effects. Thus, it extends to complete three-field two fluid equations as shown in Sec. II. In this part, two serials of equilibrium profiles in JET-like tokamak geometry with shifted circular cross section, as shown in Fig. 6, are used in our simulations.[36,37] The equilibrium density profiles are given by $n_i(\psi_{nor}) = n_e(\psi_{nor}) = n_{e0} \times P_0(\psi_{nor})^{0.3}$, assuming that the ion and electron temperatures are equal [$T_e = T_i = P_0/(2n_e)$]. Here equilibrium $P_{0,1}$ and $P_{0,2}$ in Fig. 6 are with the same central density $n_{e0} = 3 \times 10^{19}\ \mathrm{m}^{-3}$. In addition, the normalized alfvén time is

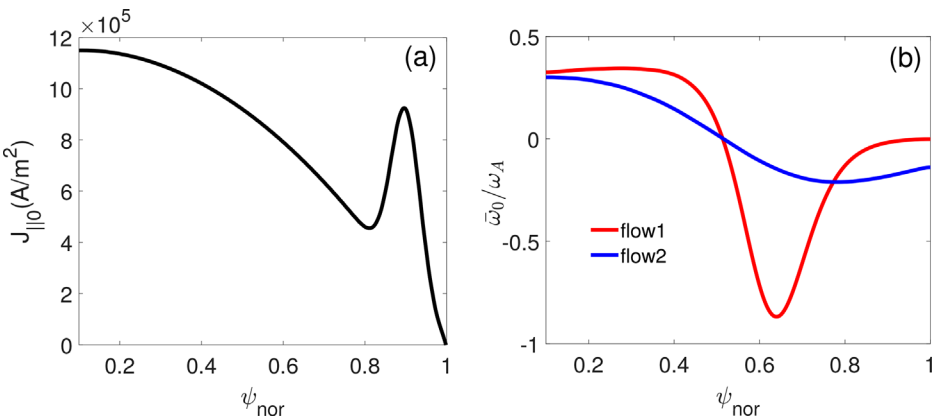


**FIG. 4.** (a) Mean parallel current profile. (b) Two mean vorticity profiles.

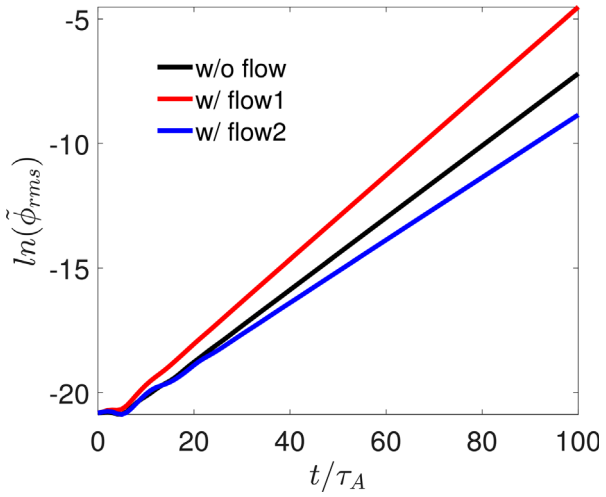


**FIG. 5.** Time evolution of the RMS of the perturbed electrostatic potential at the most unstable location of the pure kink mode. Here the toroidal mode number is n = 3.

$\tau_A = 3.36 \times 10^{-7}$ s with the reference length $\bar{R} = 3.38$ m, ion number density $n_0 = 1 \times 10^{19}\,\mathrm{m}^{-3}$, and magnetic field strength $\bar{B} = 2.06$ T, respectively. Equilibrium $P_{0,1}$ has larger pressure gradient and bootstrap current (which corresponds to larger growth rate), and it is mainly dominated by low-n Peeling–Ballooning unstable modes, so that it is much more suitable to investigate the driving effects. Equilibrium $P_{0,2}$ (dashed lines in Fig. 6) has much lower pressure and current, which is adopted to avoid ELMs (or in other words, to get saturated state) throughout the nonlinear simulations for the further study of the external torque (such as neutral beam injection).

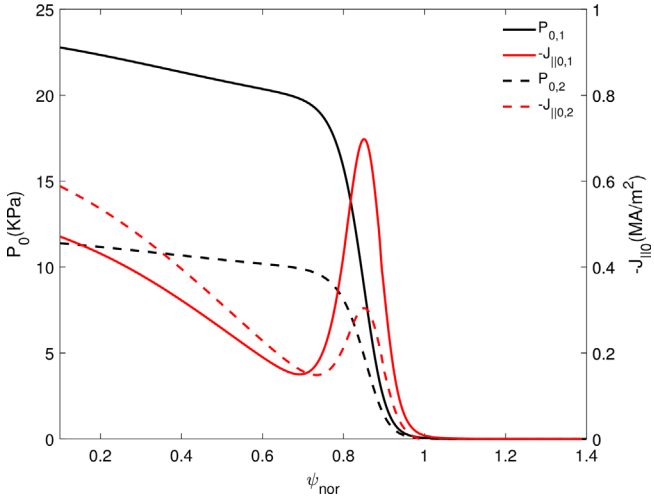


**FIG. 6.** Two serials of equilibrium profiles in JET-like Tokamak geometry including bootstrap current with a shifted circular cross section. The solid lines represent equilibrium $P_{0,1}$ and dashed lines represent equilibrium $P_{0,2}$, respectively. The equilibrium $P_{0,2}$ has the same central density as $P_{0,1}$, but only half pressure of equilibrium $P_{0,1}$.

According to the radial force balance, the total radial electric field can be expressed as

$$\begin{aligned} E_{r,total} &= E_{r,dia0} + E_{r,net} \\ &= \frac{\nabla P_i}{Z_i e n_i} - RB_p \frac{d\Phi_{V0}(\psi)}{d\psi} \\ &= \frac{\nabla P_i}{Z_i e n_i} - RB_p \{D_0 [1 - \tanh(D_s(\psi_{nor} - \psi_0))] + C\}, \end{aligned} \quad (10)$$

where the $E_{r,dia0}$ part corresponds to pressure gradient contribution, and the $E_{r,net}$ part corresponds to the net equilibrium flow contribution, respectively. First, we choose $P_{0,1}$ as the equilibrium profile, $D_0 = 45$ krad/s, $D_s = 15$, $C = 3$ krad/s, and $\psi_0 = 0.855$ (which is the largest pressure gradient location). Figure 7(a) shows the profiles of various radial electric field components at the outer mid-plane, where the diamagnetic electric field is always negative because it is determined by the pressure gradient. The electric field of net equilibrium flow can be positive or negative, depending on the net equilibrium flow in co-direction (marked as "co") or counter-direction (marked as "counter") of the ion diamagnetic flow.

The results of their corresponding linear growth rate [Fig. 7(b)] show that $E_{r,net,counter}$ will cause a stabilizing effect on the low- and medium-n modes [shifting the whole $\gamma(n)$ spectrum downwards], while $E_{r,net,co}$ will cause a destabilizing effect on these modes [shifting the whole $\gamma(n)$ spectrum upwards]. For a deeper analysis, the detailed $E_r$-shear and $E_r$-curvature of the $E_r$ profiles in Fig. 7(a) are compared in Fig. 8. From the previous arguments, we already know that $E_r$-shear tends to stabilize, while $E_r$-curvature tends to destabilize the kink modes. For the case of co-direction of ion-diamagnetic net equilibrium flow [Fig. 8(a)], we can see that the $E_r$-shear peaks at the left side of $\psi_0$ while the $E_r$-curvature is at the right side. So, it will result in a destabilizing effect on the right side and a stabilizing effect on the left side of $\psi_0$. In this case, as the $E_r$-curvature plays a dominant role, the mode structure will peak at the right side of $\psi_0$ (red curves in Fig. 9). On the other hand, for the case of counter-direction of ion-diamagnetic net equilibrium flow [Fig. 8(b)], both the $E_r$-shear and $E_r$-curvature peak at the right side of $\psi_0$. There is a competition between $E_r$-shear's stabilizing effect and $E_r$-curvature's destabilizing effect. In this case, the $E_r$-shear dominates. As a result, the mode structure will peak at the left side of $\psi_0$ (blue curves in Fig. 9).

For various types of $E_r$ profiles, we found that when the lowest point of $E_r$ shifts rightwards, $\mathcal{R}_{E_r}$ increases (i.e., the $E_r$-curvature's destabilizing effect plays a dominant role), then the MHD modes will be destabilized [Figs. 10(a) and 10(b)]. When the lowest point of $E_r$ shifts leftwards, $\mathcal{R}_{E_r}$ decreases (i.e., the $E_r$-shear's stabilizing effect plays a dominant role), then the MHD modes will be stabilized [Figs. 10(c) and 10(d)].[24] The stabilizing and destabilizing effect stem from dephasing and phase locking between $\theta_{\tilde{v}_r}$ and $\theta_{\tilde{\xi}_r}$ as discussed in Sec. III.

Second, we chose $P_{0,2}$ as the equilibrium profile to get a steady state because it has relatively small pressure gradient and it is linear stable. Then we add two different external "experimental shape" $E_r$ profiles (torques)[36] ($E_{r,torque1}$ and $E_{r,torque2}$ in Fig. 11) separately to investigate their linear and nonlinear impacts. For these two $E_r$ profiles, Fig. 12 shows that their $E_r$-shear and $E_r$-curvature both peak at the right side of $\psi_0$ (the peak of torque1's $E_r$-curvature is closer to $\psi_0$), and the ratio $\mathcal{R}_{E_r,torque1} > \mathcal{R}_{E_r,torque2}$. Therefore, we speculate that

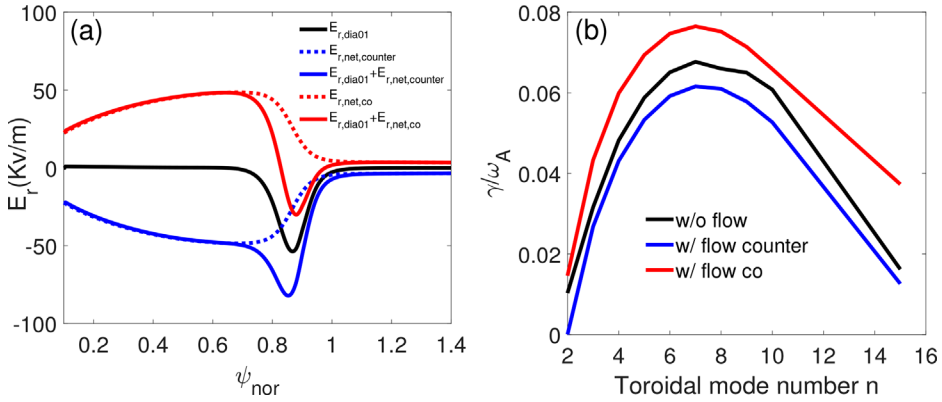


**FIG. 7.** (a) Different $E_r$ profiles' components at the outer mid-plane. (b) The corresponding growth rate spectrum. "w/o flow" (black curves) denotes without net equilibrium flow, counter (blue curves) denotes net equilibrium flow in counter-direction of ion diamagnetic flow, and "co" (red curves) denotes net equilibrium flow in co-direction of ion diamagnetic flow.

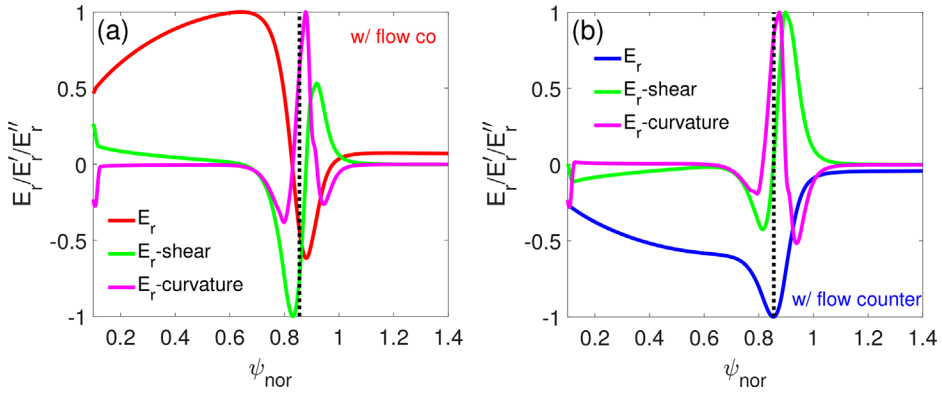


**FIG. 8.** Normalized $E_r$, $E_r$-shear, and $E_r$-curvature profiles for net equilibrium flow in the (a) co-direction and (b) counter-direction of ion diamagnetic flow. The vertical dashed line denotes the location of the largest pressure gradient.

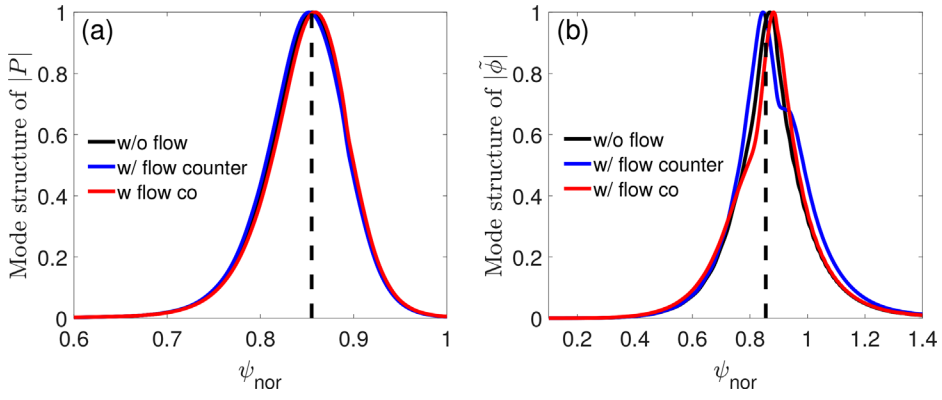


**FIG. 9.** Mode structures of the (a) perturbed pressure and (b) perturbed electrostatic potential. The toroidal mode number is $n=7$ and the vertical dashed line denotes the location of the largest pressure gradient.

$E_{r,torque1}$ will destabilize more and stronger low n modes than $E_{r,torque2}$ based on discussions from $P_{0,1}$. Figure 13(a) shows that for the case of external torque1, the linear growth rate spectrum $\gamma(n)$ concentrates on low-n modes with the most unstable mode $n=7$. For the case of external torque2, although the $E_r$-shear is moderate where the $E_r$-curvature peaks, the $E_r$-curvature plays a dominant role in determining the stability, i.e., a destabilizing effect as shown in Fig. 13(a) (blue curve), where $\gamma(n)$ concentrates on medium-n modes with the most unstable mode $n=12$. In addition, as the strength of these two $E_r$ profiles are in a comparable level, their maximum growth rate is nearly the same. It should be noted that for the medium-n modes ($n \geq 10$), they are ballooning like modes. The peak of $E_r$-shear in torque1's case is closer to the largest pressure gradient location than torque2's case; hence, its stabilization effect on these medium-n modes is stronger than torque2. As a result, the growth rate of the medium-n modes for torque1's case is smaller than that of torque2's case.

Figures 13(b)–13(d) show the mode structure of the perturbed electrostatic potential with different external torques, where the

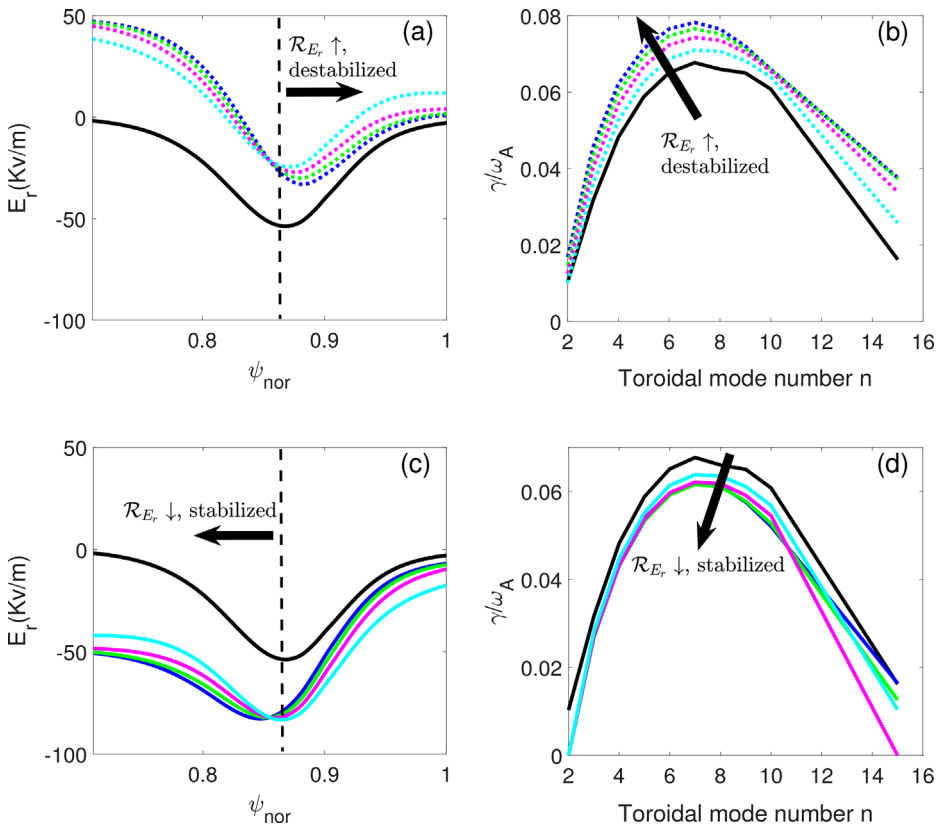


**FIG. 10.** (a) Lowest point of $E_r$ shifts rightwards, $\mathcal{R}_{E_r}$ increases, the MHD modes are destabilized as shown in (b) the corresponding linear growth rate spectrum of different $E_r$ profiles with the same color in (a). (c) Lowest point of $E_r$ shifts leftwards, $\mathcal{R}_{E_r}$ decreases, the MHD modes are stabilized as shown in (d) the corresponding linear growth rate spectrum of different $E_r$ profiles with the same color in (c). The vertical dashed line denotes the location of the largest pressure gradient.

toroidal mode number is $n=7$. The mode structure of $\Im\tilde{\phi}$ has an odd parity around the largest pressure gradient, while $\Re\tilde{\phi}$ does not show clear even or odd parity. An important point is that the destabilized unstable mode is mainly dominated by the $E_r$ curvature, whose peaks are on the right side of the largest pressure gradient location ($\psi_0$). As a consequence, both the peaks of $|\tilde{\phi}|$ in these two cases are located at the right side of $\psi_0$. In addition, the peak of torque1's $|\tilde{\phi}|$ is closer to $\psi_0$ because the peak of $E_{r,torque1}$'s $E_r$-curvature is much closer to $\psi_0$. The correlating evidence with the cases studied in this paper are qualitatively consistent with our previous results and arguments that it is the $E_r$-curvature that tends to destabilize the edge MHD modes.[24]

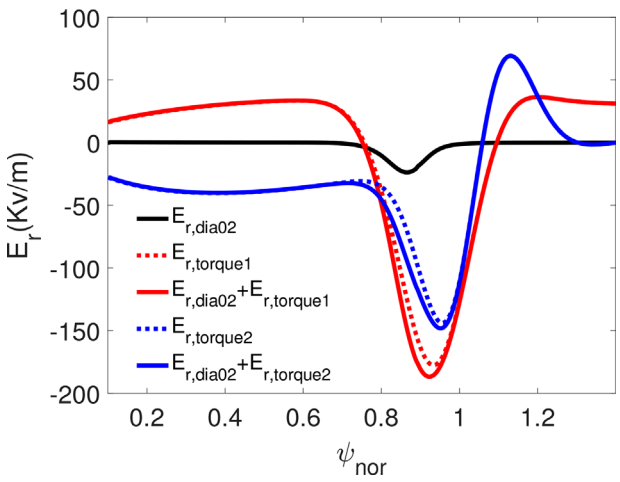


**FIG. 11.** Different $E_r$ profiles with different experimental shape components (torques) at the outer mid-plane: torque1 (red curves) and torque2 (blue curves).

In the nonlinear stage, we define a dimensionless parameter to study the property of edge energy loss fraction[38]

$$\Delta_{PED}=\frac{\Delta W_{PED}}{W_{PED}}=\frac{\int_{\psi_{in}}^{\psi_{out}}d\psi\oint Jd\theta dz'(P_0-\langle P\rangle_{z'})}{\int_{\psi_{in}}^{\psi_{out}}d\psi\oint P_0Jd\theta dz'},\qquad(11)$$

i.e., the ratio of the energy loss $\Delta W_{PED}$ to the pedestal stored energy $W_{PED}$. The lower integral limit is the pedestal inner radial boundary $\psi_{in}$, and the upper limit is the location of the largest pressure gradient location $\psi_{out}$. $P$ is the pedestal pressure at time $t$, $P_0$ is the initial pedestal pressure, and symbol $\langle\rangle_{z'}$ means the average over bi-normal periodic coordinate $z'$ [$z'=\zeta-\int_{\theta_0}^{\theta}\nu(\psi,\theta)d\theta$, where $\nu$ is the local field-line pitch]. $J^{-1}=B_\theta/h_\theta$ ($h_\theta=1/|\nabla\theta|$) is the Jacobian in the field aligned coordinate.[25] For the case without external torque, it is linear stable, so the RMS of the perturbed pressure saturated at a relatively small amplitude [black curve in Fig. 14(a)], and the energy loss fraction is nearly zero during the whole period [black curve in Fig. 14(b)]. For the case of external torque1, its narrow linear growth rate

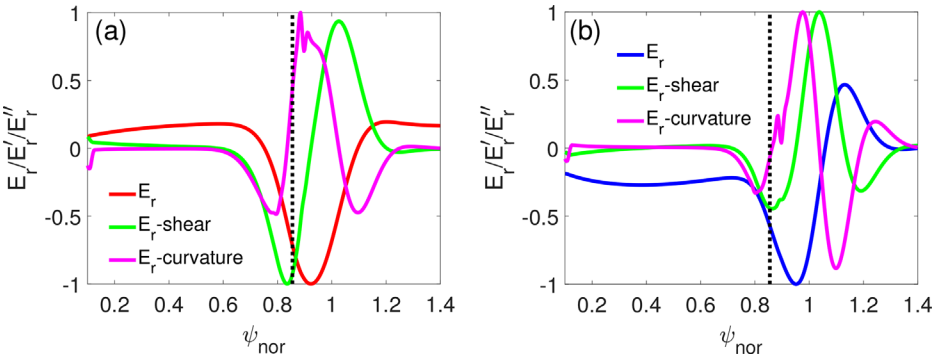


**FIG. 12.** Normalized $E_r$, $E_r$-shear and $E_r$-curvature for the case of (a) external torque1 and (b) external torque2. The vertical dashed line denotes the location of the largest pressure gradient.

spectrum leads to a weak mode–mode coupling;[29,30] thus, the fluctuations will grow for a long time in the linear stage (lasts for about 510 $\tau_A$), resulting in relatively larger saturation level [red curve in Fig. 14(a)] and energy loss fraction [red curve in Fig. 14(b)] compared with the case without external torque. For the case of external torque2, the broad linear growth rate spectrum corresponds to relatively strong mode–mode coupling. The fluctuations will grow for a shorter time (lasts for about 435 $\tau_A$) in the linear stage [blue curve in Fig. 14(a)], and the energy loss fraction [blue curve in Fig. 14(b)] is smaller compared with external torque1's case. It should be mentioned that these two cases with external torques are saturated at a comparable $P_{RMS}$ level [Fig. 14(a)] without continuous energy loss [e.g., Fig. 13(a) in Ref. 37], so it is suggested that these two ELM-free cases both may help for modest particle and energy release (especially impurity removal) to get rid of large ELM crash events.[36,37]

## V. CONCLUSION AND DISCUSSION

In this paper, we extend the concept of vorticity wave interactions to MHD systems at the edge of tokamaks. Both the current gradient and vorticity gradient could produce local vorticity waves, and they may couple to form a joint mode. We found that in the case of uniform current and vorticity distributions, stable kink mode may be destabilized by the stable mean flow, resulting in instability. Additionally, unstable kink modes may be stabilized by the mean flow.

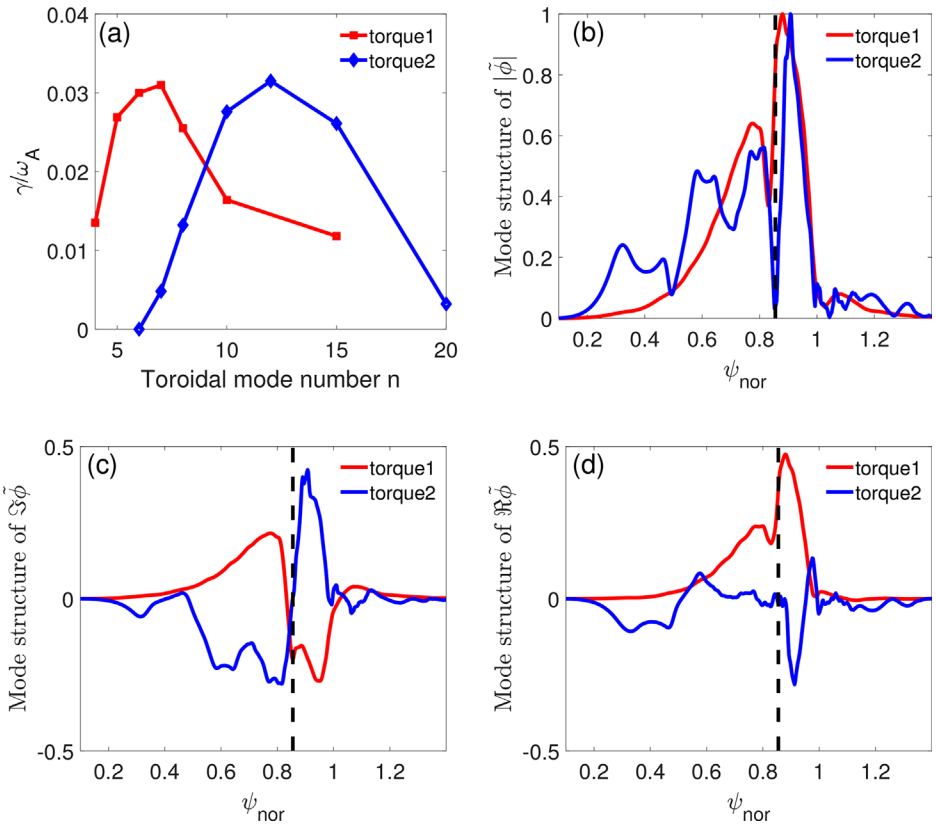


**FIG. 13.** (a) Linear growth rate spectrum of $P_{0,2}$ with external torque. Mode structures of the perturbed electrostatic potential with different external torques, which have been normalized to their respective maximum amplitude values: (b), (c), and (d) shows the radial profiles of the amplitude $|\tilde{\phi}|$, imaginary part $\Im\tilde{\phi}$ and real part $\Re\tilde{\phi}$, respectively. Here the vertical dashed line denotes the location of the largest pressure gradient, and the toroidal mode number is = 7.

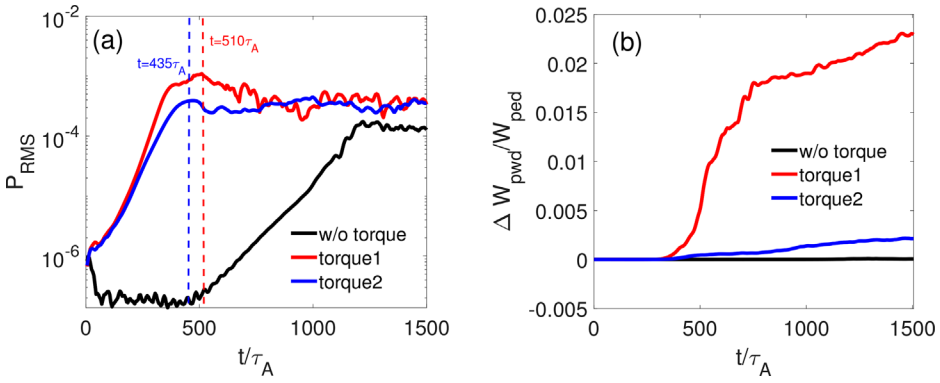


**FIG. 14.** (a) Time evolution of the RMS of the perturbed pressure at the peak equilibrium pressure gradient and outer midplane, where the vertical dashed lines mark the end of the growth stage. (b) Time evolution of the plasma energy loss fraction.

The essential physics of the joint vortex-kink mode depend on the relationship between the perturbed radial velocity and displacement. In the case of nonuniform profiles, we found that $E_r$-shear tends to stabilize the low n kink modes, while $E_r$-curvature tends to destabilize the kink modes. There is a competition between $E_r$-curvature's destabilizing and $E_r$-shear's stabilizing effect, and their ratio could be measured as a quantitative parameter. For linear low-n dominant Peeling–Ballooning unstable equilibrium, when the lowest point of $E_r$ profile shifts leftwards (rightwards), the ratio [$\mathcal{R}_{E_r}$ in Eq. (9)] between $E_r$-curvature and $E_r$-shear is smaller (larger), thus the Peeling–Ballooning modes will become more stable (unstable). For linear stable equilibrium, the larger $\mathcal{R}_{E_r}$ causes more unstable Peeling–Ballooning modes, leading to the narrower $\gamma(n)$ spectrum, and the higher nonlinear energy loss fraction.

In short, the dual role of the radial electric field $E_r$ enlightens us that a shallower $E_r$ may also has good stability if the $E_r$-shear plays a dominant role. On the other hand, even a deeper $E_r$-profile may be more unstable if $E_r$-curvature plays a dominant role. In other words, the shape of $E_r$ profile is crucial to the stability and even transport, not only the strength or depth.

By means of the analysis above, it is interesting and significant to investigate the ELM-free steady-state scenarios of real tokamak experiments. Moreover, the net poloidal flow introduced in this work will generate the parallel return flow so as to satisfy the divergence free condition $\nabla \cdot \boldsymbol{V} = 0$ in the toroidal devices, which has not been considered yet. The parallel return flow, on the one side, may drive MHD instability directly through parallel flow shear.[39,40] Conversely, the parallel return flow will modify the vorticity and vorticity gradient, which will impact the vorticity wave interaction. The investigation of the fundamental physics is an interesting question for further work. In addition, the theoretical investigation of nonlinear Peeling–Ballooning modes with external torque (flow), especially the feedback of instabilities to the equilibrium $E_r$ profiles will be our next step work in the future.

## ACKNOWLEDGMENTS

We appreciate the anonymous referees for their critical comments and constructive suggestions. We want to thank D. Hu, Z. J. Mao, Y. Lang, C. Meng, and Y. R. Zhu for useful physics discussions. We are also grateful to W. M. Chen, B. Gui, X. Chen, G. Q. Dong, and B. Dudson for useful technical help. We acknowledge fruitful interactions with participants in the Festival de Théorie, Aix-en-Provence (2019). This project was supported by the National MCF Energy R&D Program (No. 2018YFE0311400), the National Natural Science Foundation of China (Nos. 1205013, 11875124 and U1867222), the China Postdoctoral Science Foundation (No. 2021M701124), the Sichuan Youth Science and Technology Innovation Team Project (No. 2020JDTD0030) and USDOE by LLNL under No. DE-AC52–07NA27344. The numerical simulations were supported by the High-performance Computing Platform of Peking University.

## AUTHOR DECLARATIONS

### Conflict of Interest

The authors have no conflicts to disclose.

### Author Contributions

**Yi Zhang:** Conceptualization (equal); Funding acquisition (equal); Investigation (equal); Writing – original draft (equal); Writing – review & editing (equal). **Zhibin Guo:** Conceptualization (equal); Funding acquisition (equal); Supervision (lead); Writing – review & editing (equal). **Patrick Diamond:** Conceptualization (equal); Writing – review & editing (equal). **Xueqiao Xu:** Conceptualization (equal); Writing – review & editing (equal). **Zeyu Li:** Conceptualization (equal); Writing – review & editing (equal). **Min Xu:** Conceptualization (equal); Writing – review & editing (equal).

## DATA AVAILABILITY

The data that support the findings of this study are available from the corresponding author upon reasonable request.

## REFERENCES

[1]P. H. LeBlond and L. A. Mysak, Waves in the Ocean (Elsevier, 1981).
[2]I. M. Held, *Large Scale Dynamical Processes in the Atmosphere* (London: Academic Press, 1983), pp. 127–168.
[3]T. W. J. Unti and M. Neugebauer, Phys. Fluids **11**, 563 (1968).
[4]P. C. Liewer, Nucl. Fusion **25**, 543 (1985).
[5]E. Heifetz, R. Maor, and A. Guha, Q. J. R. Meteorol. Soc. **146**, 1056 (2020).
[6]J. R. Carpenter, E. W. Tedford, E. Heifetz, and G. A. Lawrence, Appl. Mech. Rev. **64**, 060801 (2011).
[7]F. Wagner, G. Becker, K. Behringer, D. Campbell, A. Eberhagen, W. Engelhardt, G. Fussmann, O. Gehre, J. Gernhardt, G. v Gierke *et al.*, Phys. Rev. Lett. **49**, 1408 (1982).

[8]K. Itoh and S.-I. Itoh, Plasma Phys. Controlled Fusion **38**(1), 1 (1996).
[9]J. W. Connor, R. J. Hastie, H. R. Wilson, and R. L. Miller, Phys. Plasmas **5**, 2687 (1998).
[10]P. B. Snyder, H. R. Wilson, J. R. Ferron, L. L. Lao, A. W. Leonard, T. H. Osborne, A. D. Turnbull, D. Mossessian, M. Murakami, and X. Q. Xu, Phys. Plasmas **9**, 2037 (2002).
[11]P. T. Lang, K. Lackner, M. Maraschek, B. Alper, E. Belonohy, K. Gál, J. Hobirk, A. Kallenbach, S. Kálvin, G. Kocsis *et al.*, Nucl. Fusion **48**, 095007 (2008).
[12]T. E. Evans, D. M. Orlov, A. Wingen, W. Wu, A. Loarte, T. A. Casper, O. Schmitz, G. Saibene, M. J. Schaffer, and E. Daly, Nucl. Fusion **53**, 093029 (2013).
[13]K. H. Burrell, M. E. Austin, D. P. Brennan, J. C. DeBoo, E. J. Doyle, C. Fenzi, C. Fuchs, P. Gohil, C. M. Greenfield, R. J. Groebner *et al.*, Phys. Plasmas **8**, 2153 (2001).
[14]M. Greenwald, R. Boivin, P. Bonoli, R. Budny, C. Fiore, J. Goetz, R. Granetz, A. Hubbard, I. Hutchinson, J. Irby *et al.*, Phys. Plasmas **6**, 1943 (1999).
[15]D. G. Whyte, A. E. Hubbard, J. W. Hughes, B. Lipschultz, J. E. Rice, E. S. Marmar, M. Greenwald, I. Cziegler, A. Dominguez, T. Golfinopoulos *et al.*, Nucl. Fusion **50**, 105005 (2010).
[16]E. Viezzer, Nucl. Fusion **58**, 115002 (2018).
[17]W. Suttrop, V. Hynönen, T. Kurki-Suonio, P. T. Lang, M. Maraschek, R. Neu, A. Stäbler, G. D. Conway, S. Hacquin, M. Kempenaars *et al.*, Nucl. Fusion **45**, 721 (2005).
[18]A. Mazurenko, M. Porkolab, D. Mossessian, J. A. Snipes, X. Q. Xu, and W. M. Nevins, Phys. Rev. Lett. **89**, 225004 (2002).
[19]J. A. Snipes, B. LaBombard, M. Greenwald, I. H. Hutchinson, J. Irby, Y. Lin, A. Mazurenko, and M. Porkolab, Plasma Phys. Controlled Fusion **43**, L23 (2001).
[20]D. F. Kong, X. Q. Xu, P. H. Diamond, J. G. Chen, C. B. Huang, T. Lan, X. Gao, J. G. Li, and EAST Team, Nucl. Fusion **59**, 016016 (2018).
[21]T. S. Hahm and K. H. Burrell, Phys. Plasmas **2**, 1648 (1995).
[22]K. Burrell, Phys. Plasmas **4**, 1499 (1997).
[23]T. Kobayashi, K. Itoh, T. Ido, K. Kamiya, S.-I. Itoh, Y. Miura, Y. Nagashima, A. Fujisawa, S. Inagaki, and K. Ida, Sci. Rep. **7**, 14971 (2017).
[24]Y. Zhang, Z. B. Guo, and P. H. Diamond, Phys. Rev. Lett. **125**, 255003 (2020).
[25]B. D. Dudson, M. V. Umansky, X. Q. Xu, P. B. Snyder, and H. R. Wilson, Comput. Phys. Commun. **180**, 1467 (2009).
[26]X. Q. Xu, B. Dudson, P. B. Snyder, M. V. Umansky, and H. Wilson, Phys. Rev. Lett. **105**, 175005 (2010).
[27]P. W. Xi, X. Q. Xu, X. G. Wang, and T. Y. Xia, Phys. Plasmas **19**, 092503 (2012).
[28]P. W. Xi, X. Q. Xu, T. Y. Xia, W. M. Nevins, and S. S. Kim, Nucl. Fusion **53**, 113020 (2013).
[29]P. W. Xi, X. Q. Xu, and P. H. Diamond, Phys. Rev. Lett. **112**, 085001 (2014).
[30]P. W. Xi, X. Q. Xu, and P. H. Diamond, Phys. Plasmas **21**, 056110 (2014).
[31]G. Q. Li, X. Q. Xu, P. B. Snyder, A. D. Turnbull, T. Y. Xia, C. H. Ma, and P. W. Xi, Phys. Plasmas **21**, 102511 (2014).
[32]B. B. Kadomtsev, *Tokamak Plasma: A Complex Physical System* (IOP Publishing Incorporated, 1992).
[33]Y. Zhang and Z. B. Guo, Plasma Sci. Technol. **23**, 045101 (2021).
[34]J. W. Connor, R. J. Hastie, and J. B. Taylor, Proc. R. Soc. London, Ser. A **365**, 1 (1979).
[35]S. J. P. Pamela, A. Bhole, G. T. A. Huijsmans, B. Nkonga, M. Hoelzl, I. Krebs, and E. Strumberger, Phys. Plasmas **27**, 102510 (2020).
[36]J. G. Chen, X. Q. Xu, C. H. Ma, P. W. Xi, D. F. Kong, and Y. A. Lei, Phys. Plasmas **24**, 050704 (2017).
[37]Y. Zhang, Z. B. Guo, X. Q. Xu, and J. G. Chen, Phys. Plasmas **26**, 052508 (2019).
[38]X. Q. Xu, J. F. Ma, and G. Q. Li, Phys. Plasmas **21**, 120704 (2014).
[39]M. Sasaki, K. Itoh, Y. Kosuga, J. Dong, S. Inagaki, T. Kobayashi, J. Cheng, K. Zhao, and S.-I. Itoh, Nucl. Fusion **59**, 066039 (2019).
[40]J. Cheng, J. Dong, K. Itoh, S.-I. Itoh, L. Yan, J. Xu, M. Jiang, Z. Huang, K. Zhao, Z. Shi *et al.*, Nucl. Fusion **60**, 046021 (2020).